Tunable Shear Thickening in Suspensions

Neil Y.C. Lin[a,1], Christopher Ness[b], Michael E. Cates[c], Jin Sun[b], and Itai Cohen[a]

[a]Department of Physics, Cornell University, Ithaca, New York 14853; [b]School of Engineering, University of Edinburgh, Edinburgh EH9 3JL, United Kingdom; [c]DAMTP, University of Cambridge, Centre for Mathematical Sciences, Wilberforce Road, Cambridge CB3 0WA, United Kingdom

Shear thickening, an increase of viscosity with shear rate, is a ubiquitous phenomena in suspended materials that has implications for broad technological applications. Controlling this thickening behavior remains a major challenge and has led to empirical strategies ranging from altering the particle surfaces and shape to modifying the solvent properties. However, none of these methods allow for tuning of flow properties during shear itself. Here, we demonstrate that by strategic imposition of a high-frequency and low-amplitude shear perturbation orthogonal to the primary shearing flow, we can largely eradicate shear thickening. The orthogonal shear effectively becomes a regulator for controlling thickening in the suspension, allowing the viscosity to be reduced by up to two decades on demand. In a separate setup, we show that such effects can be induced by simply agitating the sample transversely to the primary shear direction. Overall, the ability of in situ manipulation of shear thickening paves a route towards creating materials whose mechanical properties can be controlled.

rheology | colloidal suspensions | shear thickening | flow control

The viscosity of a densely packed suspension of particles can increase radically when sheared beyond a critical stress [1, 2]. This thickening behavior has been exploited in technological applications ranging from vehicle traction control to flexible spacesuits that protect astronauts from micrometeorite impacts [3–5]. It may also lead to flow problems such as pipe blockage during industrial extrusion processes [6]. Shear thickening has generally been considered an inherent material property [7], rather than as a response that can be tuned. As a consequence, suspension process design is often constrained within tight bounds to avoid thickening [8], while the applications of such flow behavior are limited by a lack of tunability.

To design our control method, we take advantage of the underlying shear thickening mechanisms that have been revealed recently. Experiments and simulations have shown that when the stress applied to a suspension of micron-sized particles exceeds a critical value, the particle-particle interaction switches from lubricated to frictional, enhancing resistance to flow [6, 9–13]. The stress is transmitted through shear-induced force chains, which arise from frictional particle contacts [6, 13–15], aligned along the compressive axis. Such chains are fragile [16, 17] and are constantly broken and rebuilt during steady shear.

This fragility paradigm asserts that these stress-transmitting chains are themselves a product of the stress, with a finite chain-assembly time required following startup or perturbations to the flow direction [18, 19]. These insights suggest a strategy for controlling thickening. For perturbations slower than chain assembly, contact rearrangement is sufficiently fast that force chains remain aligned with the instantaneous net compressive axis. Conversely, for perturbations faster than the assembly time, chains cannot reach

compatibility with the instantaneous net compressive axis, but occupy a partially-assembled transient state, illustrated in Fig. 1(a). The alignment of the perturbed or tilted chain deviates from the net compressive axis and it no longer transmits stresses effectively. Thus it should be possible to precisely regulate the thickening behavior by applying appropriate lateral perturbations.

To that end we design a *biaxial* shear protocol that uses an orthogonal flow perturbation to interfere with force chains induced by a primary shearing flow. Our strategy is to maximize the perturbation influence so the force chains usually responsible for thickening cannot establish fully. We conduct biaxial rheometry experimentally and numerically, mapping the response of a hard-sphere suspension as the perturbation rate and amplitude are systematically varied. By integrating our knowledge of the force chain alignment, mechanical instability and direct link to the viscosity, we show how this strategy can be optimized. We focus on *discontinuous* shear thickening suspensions, as their vast viscosity variations make them most problematic to the engineer [10, 11, 20]. Our results show that through suitable regulation, the suspension viscosity at a fixed flow rate may be reduced by up to two decades in an active and controlled manner. We finally demonstrate the wide utility of the technique using a simpler flow regulation set up.

The biaxial rheometry experiment is performed using a double-wall Couette geometry that has an outer cup driven continuously by an underneath motor, and an inner bob attached to an oscillating shaft [21–23]. A simplified schematic and coordinate definition are shown in Fig. 1(b). The continuous primary flow in the $\hat{r}\hat{\theta}$ plane along the $\hat{\theta}$ direction, at

Significance Statement

When a concentrated suspension is strained, its viscosity can increase radically. This behavior, known as shear thickening, can be very useful to technological applications or highly problematic in industrial processes. Suspension flow properties are typically specified at the formulation stage, meaning they are fixed in advance rather than controlled in situ during application. Here, we report a biaxial shear strategy eradicating the flow induced structures responsible for thickening, and tuning the suspension viscosity on demand during flow. This protocol enables us to regulate the thickening viscosity over two-orders of magnitude. The tuning capability is a foundational step toward employing dense suspensions in 3D printing, energy storage, and robotics.
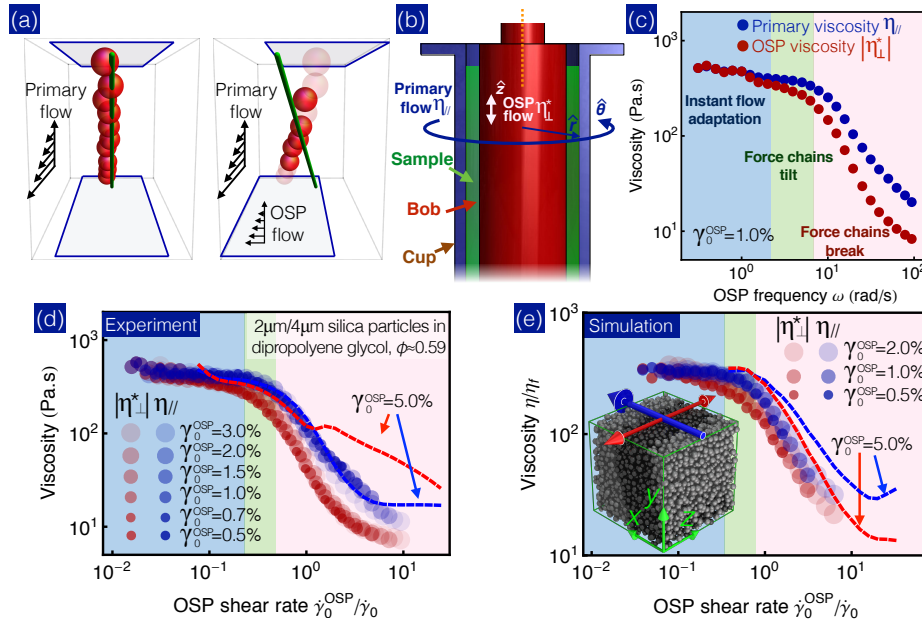
Fig. 1. Perturbing the frictional force chains that govern shear thickening by imposing orthogonal shear can reduce the suspension viscosity by nearly two decades. (a) Schematic showing force chain alignment during flow. Left panel: Under simple, uniaxial shear, particles (red spheres) naturally align along the compressive axis (green line); Right panel: Under rapid biaxial shear, with transverse flow indicated by the shifted upper plate, the orthogonal perturbations may tilt or break the chains, so that they deviate from the combined compressive axis. (b) Schematic of experimental apparatus showing the continuous primary flow that drives shear thickening and the inner oscillatory module that perturbs the force chains; (c) Frequency sweep experimental data for γ_0^{OSP}=1%. Shown are the primary viscosity ($\eta_\parallel$, blue dots) and orthogonal complex viscosity ($|\eta_\perp^*|$, red dots); (d) Experimental and (e) simulation viscosity data collapse as function of the relative OSP shear rate ($\dot{\gamma}_0^{\text{OSP}}/\dot{\gamma}_0$), for several γ_0^{OSP}. Dashed lines indicate reentrant thickening when the OSP strain becomes large enough to induce new force chains; Inset (e), snapshot of simulation configuration, indicating the coordinate definitions with respect to the primary (blue arrow) and OSP (red arrows) flow directions. Further details and characterization of experimental sample can be found in Method and SI.

controlled rate $\dot{\gamma}_0$, constantly induces force chains, sets the initial shear thickening state, and probes the parallel viscosity, $\eta_\parallel$. Concurrently, an orthogonal superimposed perturbation (OSP) comprising oscillatory flow in the $\hat{r}\hat{z}$ plane along the $\pm\hat{z}$ direction perturbs the suspension by imposing a deformation $\gamma^{\text{OSP}} = \gamma_0^{\text{OSP}}\sin(\omega t)$ with rate $\dot{\gamma}^{\text{OSP}} = \omega\gamma_0^{\text{OSP}}\cos(\omega t)$, and simultaneously probes its orthogonal complex viscosity, $|\eta_\perp^*|$. Given the employed Couette cell dimension, we approximate the primary flow as a uniaxial shear in parallel plate geometry[1]. Further details about the geometry and OSP calibration can be found in Method and SI.

Following the above reasoning, we take the primary shear timescale $1/\dot{\gamma}_0$ and the OSP period $1/\omega$ as proxies for chain-assembly and perturbation times, respectively. We fix the primary shear rate at $\dot{\gamma}_0 = 0.2$ s^{-1}, where the suspension is normally strongly thickened (see SI), and conduct an OSP frequency sweep at a fixed strain amplitude $\gamma_0^{\text{OSP}} = 1\%$. The evolutions of $\eta_\parallel$ and $|\eta_\perp^*|$ are given in Fig. 1(c).

At low frequencies $\omega \leq 2$ rad/s (blue area, Fig. 1(c)), $\eta_\parallel$ and $|\eta_\perp^*|$ exhibit plateaus that match the original thickening viscosity ~ 500 Pa.s, for $\gamma_0^{\text{OSP}} = 0$ (see SI). In this regime, the primary flow renews the force chains rapidly so that they are always compatible with the net compressive axis, and their alignment appears to adapt instantly to the OSP flow. This instantaneous adaptation gives rise to an isotropic and unaffected thickening behaviour (see SI for an analytical derivation). As the frequency increases to 2 rad/s < $\omega \leq 8$ rad/s (green area), we find that the OSP viscosity $|\eta_\perp^*|$ decays slightly, while the primary value $\eta_\parallel$ remains relatively constant

(within 7%). The decay in $|\eta_\perp^*|$ suggests that the OSP flow deforms or tilts existing force chains more quickly than they are replaced by new ones, while the unchanged $\eta_\parallel$ suggests the tilted chains remain largely intact. Finally, we observe a substantial drop in both $\eta_\parallel$ and $|\eta_\perp^*|$ at even higher frequencies $\omega > 8$ rad/s implying significant breakage of force chains and dissolution of the flow induced contact network. Qualitatively, this result is consistent with our above interpretation of the fragile, marginally stable nature of the force chain network, and reaffirms the link between the stress bearing capability of the chains, and the viscosity of the suspension [11].

To further elucidate the roles being played by the primary and OSP flows, we repeat the frequency sweep measurement at six different γ_0^{OSP}, Fig. 1(d). We normalize the OSP shear rate magnitude by the primary rate $\dot{\gamma}_0^{\text{OSP}}/\dot{\gamma}_0 (= \omega\gamma_0^{\text{OSP}}/\dot{\gamma}_0)$, and find that all $\eta_\parallel$ and $|\eta_\perp^*|$ data, for $\gamma_0^{\text{OSP}} < 5\%$, collapse onto two master curves (blue and red dots, respectively). Furthermore, the onset of the chain breaking regime occurs at $\dot{\gamma}_0^{\text{OSP}}/\dot{\gamma}_0 \approx 1$. This scaling suggests that the force chain response, whether they instantly adapt to the OSP flow, tilt, or break, is determined by the competition between $\dot{\gamma}_0^{\text{OSP}}$ and $\dot{\gamma}_0$. While $\dot{\gamma}_0$ indicates how frequently force chains reform, $\dot{\gamma}_0^{\text{OSP}}$ dictates how rapidly the OSP flow perturbs these structures. In other words, the ratio $\dot{\gamma}_0^{\text{OSP}}/\dot{\gamma}_0$ directly governs the viscosity reduction of a biaxially sheared sample. For large γ_0^{OSP} (>5%), we observe a deviation from the master curves, suggesting a possible reentrant thickening arising when chains induced by the OSP flow emerge. We conclude, therefore, that for sufficiently large $\dot{\gamma}_0^{\text{OSP}}/\dot{\gamma}_0$ and sufficiently small γ_0^{OSP}, our orthogonal flow perturbation disrupts the conventional shear-induced contact network, inhibiting friction-mediated force chains and

[1] Note that uniaxial *shear* as defined here is technically a biaxial *flow* since there is no axis of rotational symmetry
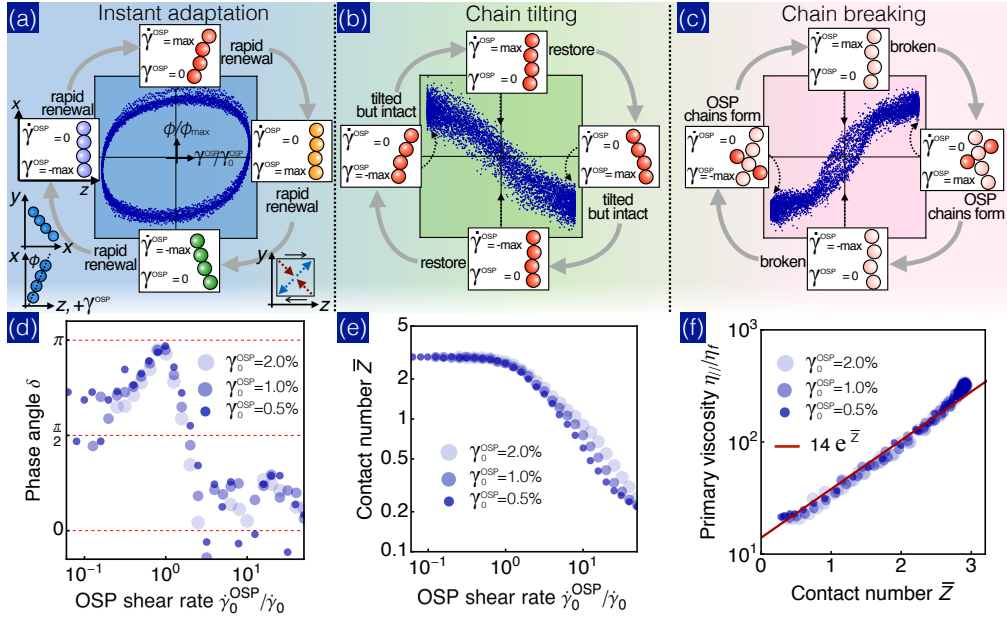
Fig. 2. Microstructural information from simulations to illustrate the mechanism behind the viscosity reduction with increased OSP flow, for $\gamma_0^{\mathrm{OSP}} = 1\%$. Shown are Lissajous curves for microstructural force chain alignment for the (a) instant adaptation, (b) chain tilting and (c) chain breaking regimes, with ϕ and γ^{OSP} normalized by their maximal values, where $\phi_{\max} \sim \mathcal{O}(10^{-2})$. ϕ and the sign of γ^{OSP} are defined in the Left Inset of (a), and definitions of compression (red) and extension (blue) quadrants of the OSP flow in Right Inset of (a), for positive $\dot\gamma^{\mathrm{OSP}}$. Force chain diagrams in (a), (b), (c) illustrate alignment projected to $\hat{x}\hat{z}$ at each stage of the oscillatory cycle, while alignment in $\hat{x}\hat{y}$ remains along the compressive axis of the primary flow throughout (Left Inset of (a)); (d) Evolution of phase angle δ between ϕ and γ^{OSP} with OSP shear rate, where $\delta = 0$ and $\delta = \pi/2$ respresent elastic and viscous responses respectively; (e) Evolution of time-averaged contact number $\bar{Z}$ with OSP shear rate; (f) Direct dependence of primary flow viscosity on time-averaged contact number $\bar{Z}$.

mitigating shear thickening. The extent of this mitigation may be set using $\dot\gamma_0^{\mathrm{OSP}}/\dot\gamma_0$ as a control parameter, allowing precise *regulation* of the viscosity of dense suspensions.

To clarify the detailed microstructural rearrangements leading to the observed measurements we use numerical simulations, explicitly resolving the trajectories and interactions of suspended, bidisperse spheres (diameter ratio 1:1.4) using a classical discrete element code [24, 25] enhanced with the recently established Critical Load Model [15, 26]. Hydrodynamic forces are approximated as pairwise lubrication interactions (viscosity η_f) between neighboring particles, while particle contacts are treated as linear springs with friction appearing above a critical normal force. The fixed-volume fraction (55%), periodic, Cartesian simulation cell can be deformed to simulate steady shear in a primary direction with a small amplitude oscillation in the orthogonal direction. With respect to the illustration in Fig 1(e), primary flow (blue arrow) is in the $\hat{x}\hat{y}$ plane, along the $\hat{x}$ direction, and OSP flow (red arrows) is in the $\hat{y}\hat{z}$ plane, along the $\pm\hat{z}$ direction. Full details and discussion of model assumptions are given in SI.

The experimental flow measurements are repeated computationally with consistent results, shown in Fig. 1(e). The force chain alignment is interrogated in the three identified regimes, instant adaptation, chain tilting, and chain breaking. In all regimes, the chains lie mainly along the compressive axis of the primary shear flow, but are subtly shifted out of the $\hat{x}\hat{y}$ plane by the OSP flow. To quantify these deviations, we calculate a fabric tensor $\langle \hat{r}_i^{\alpha\beta} \hat{r}_j^{\alpha\beta} \rangle$ capturing the particle contact configuration [14], where $r_i^{\alpha\beta}$ ($\alpha \neq \beta$) is the unit vector between particles α and β, while i, j denote the coordinate indices and $\langle \ldots \rangle$ denotes the average over all neighboring particles. We take $\phi = \tan^{-1}(\langle \hat{r}_y \hat{r}_z \rangle / \langle \hat{r}_x \hat{r}_y \rangle)$ as the angle between the force

chains and x-axis, when projected to $\hat{x}\hat{z}$, Fig 2a (Left Inset), which remains small, $\phi_{\max} \sim \mathcal{O}(10^{-2})$, throughout. Chains inclined towards the compressive quadrant of the OSP flow (see Right Inset, Fig 2a) have positive ϕ for positive $\dot\gamma^{\mathrm{OSP}}$.

Representative Lissajous curves of $\phi(\gamma^{\mathrm{OSP}})$ for the three regimes are shown in Fig. 2(a), (b), and (c), for time-varying OSP strain γ^{OSP}. For low OSP rates $\dot\gamma_0^{\mathrm{OSP}}/\dot\gamma_0 \ll 1$, newly formed force chains always align with the net compressive axis dictated by the instantaneous combined flow, so ϕ is in phase with the time-varying OSP *strain rate*, $\phi \propto \dot\gamma^{\mathrm{OSP}}$, Fig. 2(a), generating isotropic thickening as reported in Fig. 1(d) and (e). For $\dot\gamma_0^{\mathrm{OSP}}/\dot\gamma_0 \approx 1$, the time scales for the OSP and primary flows are comparable, so it is expected that chains are tilted before they can rearrange. Indeed, we find that chain alignment is antiphase to the OSP *strain*, $\phi \propto -\gamma^{\mathrm{OSP}}$, Fig. 2(b). This indicates that rather than adapting to the instantaneous flow rate, existing force chains are instead tilted affinely by the transverse deformation (strain) and occupy the extensional quadrant of the OSP flow while $\gamma^{\mathrm{OSP}} \neq 0$, as sketched in Fig 1a (right panel). When the OSP rate dominates $\dot\gamma_0^{\mathrm{OSP}}/\dot\gamma_0 \gg 1$, the affine deformation caused by the transverse flow is fast enough to break these tilted force chains more rapidly than the primary flow is able to sustain or re-establish them. Meanwhile, new contacts may be formed by the OSP flow in its compressive quadrant. Thus, the chain alignment is in phase with the OSP strain $\phi \propto \gamma^{\mathrm{OSP}}$, Fig. 2(c). The implication of the final curve is striking. In the chain breaking regime, the thickening becomes solely governed by the strain amplitude of the OSP flow. We summarize the chain alignment behavior by plotting the phase lag δ between ϕ and γ^{OSP} in Fig. 2(d).

Since the shear thickened viscosity directly arises from frictional particle contacts [12], we expect that the evolution of the

force chain response with increasing $\dot{\gamma}_0^{\mathrm{OSP}}/\dot{\gamma}_0$ is accompanied by a reduction in particle contacts. To verify this, we calculate the time-averaged per-particle coordination number $\bar{Z}$. We find that $\bar{Z}(\gamma_0^{\mathrm{OSP}}, \omega)$ collapses in a similar fashion to the measured viscosity, and starts to decay around $\dot{\gamma}_0^{\mathrm{OSP}}/\dot{\gamma}_0 \approx 1$, Fig. 2(e). Indeed, plotting $\eta_\parallel$ versus $\bar{Z}$ we recover a simple relationship $\ln \eta \propto \bar{Z} + \mathrm{const}$, Fig. 2(f). When no particle contact is formed, $\eta_\parallel$ corresponds to the viscosity purely arising from the interparticle hydrodynamic interactions [27]. As $\bar{Z}$ increases, $\eta_\parallel$ rises and brings more particles into contact, which in turn produces a higher viscosity. Overall, these simulations reaffirm the bulk rheological effect of the orthogonal perturbation and reveal the microstructural mechanism by which the OSP flow can manipulate the force chains to ultimately eradicate the frictional contacts responsible for shear thickening.
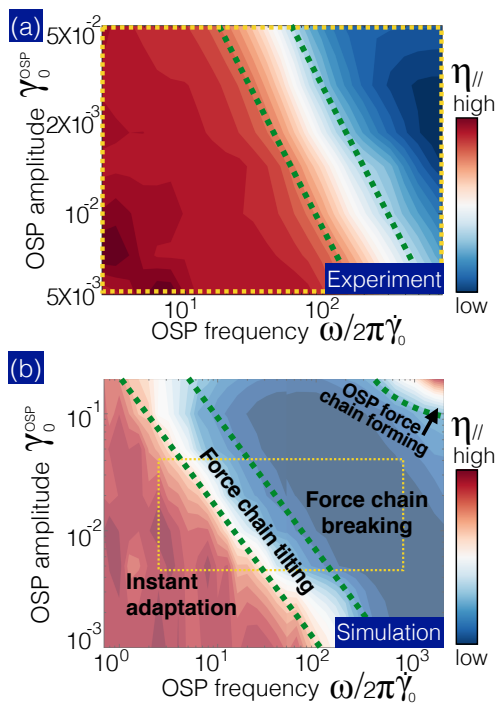

Fig. 3. Regime maps for strategic suspension viscosity regulation. Data are obtained from (a) experiments and (b) simulations. In (b), we delineate each of the phenomenological shear thickening regimes. Color scale represents primary flow viscosities. The yellow dashed box indicates the regime explored in experiment. In both experiment and simulation, the onset of viscosity reduction occurs at $\dot{\gamma}_0^{\mathrm{OSP}}/\dot{\gamma}_0 \approx 1$. This indicates that the state of the biaxially sheared suspension is determined by the competition between primary and OSP flow rates.

We construct a summary phase diagram recapitulating our strategy for tuning shear thickening, giving experimental and simulated primary viscosities as functions of γ_0^{OSP} and ω in Fig. 3(a) and (b), respectively. When an OSP flow is applied, its shear rate $\gamma_0^{\mathrm{OSP}}\omega$ determines the force chain behavior and the state of thickening in the suspension. The force chain behavior shows a transition from instant adaptation, chain tilting, to chain breaking as the OSP flow rate increases. When the OSP flow rate is even higher, however, the OSP flow may start to induce force chains by itself for sufficiently large γ_0^{OSP}. A reentrant thickening behavior is then observed, as indicated by the curved contours and red region in the upper right corners of Fig. 3(a) and (b), respectively.
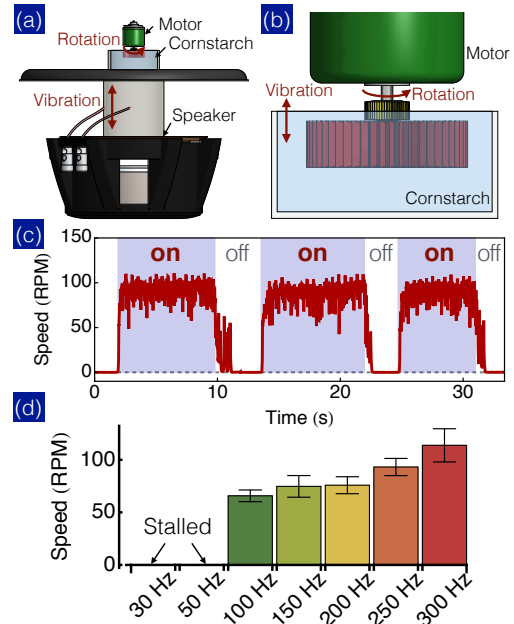

Fig. 4. A simple flow regulation set up comprising a rotating gear submerged in a cornstarch suspension illustrates the broad utility of our control scheme. Schematic of improvised flow regulator, showing (a) the full setup including driving motor, cornstarch reservoir and speaker and (b) a close-up of the setup. (c) The motor starts to rotate when the vibration (250 Hz) switches on (shaded areas), and stalls when the vibration is off. Shown in (d) is the rotation speed of the motor as a function of vibration frequency at a fixed speed. The motor remains stalled at the frequencies ≤ 50 Hz.

The orthogonal flow induced viscosity reduction allows us to drive the material at a higher speed with the same amount of driving force. In some practical cases, our biaxial protocol or a comparable oscillatory perturbation should be able to thin the suspension and effectively increase the flow processing speed. We test this prediction in a dense cornstarch suspension (solid fraction ≈ 40 wt %) [20, 28] using a simple setup consisting of a motor driven at a constant voltage and a speaker, as shown by the schematics in Fig. 4 (a) and (b). Upon motor startup, the rotating gear on the shaft immediately thickens the cornstarch, generating a large resistance that substantially slows down the gear speed. When the gear speed is below a threshold, the motor stalls. We then use the speaker to apply a high frequency and small amplitude (250Hz, 18 μm) vibration along the vertical direction to break the force chains against the gear. As a result, the motor under the same applied voltage starts to rotate again and drive the material, see Fig.4(c) and SI video. This transition repeats reversibly as we switch the speaker on and off. We also find that the motor rotation speed is maximized when we raise the vibration frequency and lower its amplitude, keeping the induced rate, analogous to $\dot{\gamma}_0^{\mathrm{OSP}}$, fixed Fig. 4(d). This finding suggests that the state of the system is in the dark blue channel in the phase diagram (Fig. 3). This channel runs upper left to bottom right indicating larger viscosity reductions at higher frequencies when the shear rate is fixed. Finally, we replace the motor with a stress-controlled rheometer (TA-Instrument DHR-3), which can rotate at a much slower rate without stalling, and repeat the speaker experiment (see SI). In this modified demonstration, the impeller on the rheometer rotates slowly when the vibration is off, and speeds up as the vibration

is turned on. We can control such a transition between slow and fast rotations by simply switching the speaker vibration. These simple demonstrations show that our strategy for using orthogonal flows to control thickening is robust, and can be realized even in less controlled settings.

In conclusion, we have, for the first time, employed a biaxial shear protocol to tune the shear thickening viscosity of a suspension. Such a control is achieved by applying a transverse perturbation that regulates the main flow, along the lines of a mechanical transistor. This contrasts with passive control in which the rheological response is set when formulating the suspension and not changed thereafter. By scaling the flow measurement data and numerically investigating the force chain behavior, we elucidate the underlying mechanism of our control method and demonstrate how it can be strategically utilized. This result might inform extension of a three-dimensional continuum description so far limited to the $\dot\gamma_0^{\mathrm{OSP}}/\dot\gamma_0 \ll 1$ regime [29]. Using a simpler flow regulation set up, we finally demonstrate that the insight obtained here can inform practical strategies, e.g., to unclog blockages caused by thickening during paste extrusion [30], 3D printing suspensions [31], and flow of carbon black in energy storage devices [32], and, more generally, to control bistability in granulation [33] and jamming in hopper flow [34]. In general, control over a fluid's rheological properties holds the promise for advancing actuation and motion controls [35, 36], which have applications ranging from controllable dampers [35], robotic arms [35, 37], to actuating orthoses [38].

Materials and Methods

The experiment is performed using an ARES-G2 rheometer (TA Instrument) in conjunction with an orthogonal superimposed perturbation (OSP) module [21, 22]. During the experiment, the parallel ($\eta_\parallel$) and orthogonal ($|\eta_\perp^*|$) viscosities of the sample are measured by strain gauges on the upper shaft. The tested suspension comprises silica particles in dipropylene glycol (Sigma-Aldrich). The sample volume fraction $\phi \approx 0.59$ is determined by directly imaging the suspension structure with a confocal microscope. The suspended particles are binary (2μm/4μm diameters) with number ratio roughly 1:1, mitigating crystallization. Our sample shear thickens at a relatively low shear rate due to the high solvent viscosity $\eta_0 = 84$ m.Pa, minimizing the instrumental instability in the biaxial test. For further characterizations of the sample structure and rheological properties, see SI.

The experimental volume fraction of 59% is chosen to represent an upper limit at which steady flow in the shear thickening regime is observed. Numerically, we are able to reproduce the uniaxial experimental rheology at 55% volume fraction. In future work we may address this difference by improving volume fraction measurement [39] and characterising particle friction [9], both of which remain interesting experimental challenges.

1. Wagner NJ, Brady JF (2009) Shear thickening in colloidal dispersions. *Physics Today* 62(10):27–32.
2. Guy B, Hermes M, Poon W (2015) Towards a unified description of the rheology of hard-particle suspensions. *Physical Review Letters* 115(8):088304.
3. Wagner NJ, Wetzel ED (2007) Advanced body armor utilizing shear thickening fluids. US Patent 7,226,878.
4. Lee YS, Wetzel ED, Wagner NJ (2003) The ballistic impact characteristics of kevlar® woven fabrics impregnated with a colloidal shear thickening fluid. *Journal of Materials Science* 38(13):2825–2833.
5. Cwalina CD (2016) Ph.D. thesis (University of Delaware).
6. Brown E, Jaeger HM (2014) Shear thickening in concentrated suspensions: phenomenology, mechanisms and relations to jamming. *Reports on Progress in Physics* 77(4):046602.
7. Brown E et al. (2010) Generality of shear thickening in dense suspensions. *Nature Materials* 9(3):220–224.
8. Benbow J, Bridgwater J (1993) *Paste flow and extrusion.* (Oxford University Press).
9. Fernandez N et al. (2013) Microscopic mechanism for shear thickening of non-brownian suspensions. *Phys. Rev. Lett.* 111:108301.
10. Seto R, Mari R, Morris JF, Denn MM (2013) Discontinuous shear thickening of frictional hard-sphere suspensions. *Physical Review Letters* 111(21):218301.
11. Wyart M, Cates M (2014) Discontinuous shear thickening without inertia in dense non-brownian suspensions. *Physical Review Letters* 112(9):098302.
12. Lin NY et al. (2015) Hydrodynamic and contact contributions to continuous shear thickening in colloidal suspensions. *Physical Review Letters* 115(22):228304.
13. Brown E, Jaeger HM (2012) The role of dilation and confining stresses in shear thickening of dense suspensions. *Journal of Rheology* 56(4):875–923.
14. Bi D, Zhang J, Chakraborty B, Behringer R (2011) Jamming by shear. *Nature* 480(7377):355–358.
15. Mari R, Seto R, Morris JF, Denn MM (2014) Shear thickening, frictionless and frictional rheologies in non-brownian suspensions. *Journal of Rheology* 58(6):1693–1724.
16. Cates M, Wittmer J, Bouchaud JP, Claudin P (1998) Jamming, force chains, and fragile matter. *Physical Review Letters* 81(9):1841.
17. Majmudar TS, Behringer RP (2005) Contact force measurements and stress-induced anisotropy in granular materials. *Nature* 435(7045):1079–1082.
18. Gadala-Maria F, Acrivos A (1980) Shear-induced structure in a concentrated suspension of solid spheres. *Journal of Rheology* 24(6):799–814.
19. Ness C, Sun J (2016) Two-scale evolution during shear reversal in dense suspensions. *Physical Review E* 93(1):012604.
20. Fall A, Huang N, Bertrand F, Ovarlez G, Bonn D (2008) Shear thickening of cornstarch suspensions as a reentrant jamming transition. *Physical Review Letters* 100(1):018301.
21. Vermant J, Walker L, Moldenaers P, Mewis J (1998) Orthogonal versus parallel superposition measurements. *Journal of Non-Newtonian Fluid Mechanics* 79(2):173–189.
22. Vermant J, Moldenaers P, Mewis J, Ellis M, Garritano R (1997) Orthogonal superposition measurements using a rheometer equipped with a force rebalanced transducer. *Review of Scientific Instruments* 68(11):4090–4096.
23. Jacob AR, Poulos AS, Kim S, Vermant J, Petekidis G (2015) Convective cage release in model colloidal glasses. *Physical Review Letters* 115(21):218301.
24. Cundall PA, Strack ODL (1979) A discrete numerical model for granular assemblies. *Géotechnique* 29(1):47–65.
25. Plimpton S (1995) Fast parallel algorithms for short-range molecular dynamics. *Journal of Computational Physics* 117(1):1–19.
26. Ness C, Sun J (2016) Shear thickening regimes of dense non-brownian suspensions. *Soft Matter* 12(3):914–924.
27. Cheng Z, Zhu J, Chaikin PM, Phan SE, Russel WB (2002) Nature of the divergence in low shear viscosity of colloidal hard-sphere dispersions. *Physical Review E* 65(4):041405.
28. Fall A, Bertrand F, Ovarlez G, Bonn D (2012) Shear thickening of cornstarch suspensions. *Journal of Rheology* 56(3):575–591.
29. Ovarlez G, Barral Q, Coussot P (2010) Three-dimensional jamming and flows of soft glassy materials. *Nature Materials* 9(2):115–119.
30. Patil PD, Feng JJ, Hatzikiriakos SG (2006) Constitutive modeling and flow simulation of polytetrafluoroethylene (ptfe) paste extrusion. *Journal of Non-Newtonian Fluid Mechanics* 139(1):44–53.
31. Sun K et al. (2013) 3d printing of interdigitated li-ion microbattery architectures. *Advanced Materials* 25(33):4539–4543.
32. Fan FY et al. (2014) Polysulfide flow batteries enabled by percolating nanoscale conductor networks. *Nano Letters* 14(4):2210–2218.
33. Cates ME, Wyart M (2014) Granulation and bistability in non-brownian suspensions. *Rheologica Acta* 53(10):755–764.
34. Damond E (1939) Apparatus for the automatic unclogging of hoppers. US Patent 2,174,348.
35. Stanway R, Sproston J, El-Wahed A (1996) Applications of electro-rheological fluids in vibration control: a survey. *Smart Materials and Structures* 5(4):464.
36. Mavroidis C, Pfeiffer C, Mosley M (2000) Conventional actuators, shape memory alloys, and electrorheological fluids in *Automation, Miniature Robotics, and Sensors for Nondestructive Testing and Evaluation*, eds. Bar-Cohen Y, for Nondestructive Testing AS. (American Society for Nondestructive Testing).
37. Tan K et al. (2002) A simple one dimensional robot joint based on the ER linear reversing mechanism. *Journal of Intelligent Material Systems and Structures* 13(7-8):533–537.
38. Nikitczuk J, Weinberg B, Mavroidis C (2005) Rehabilitative knee orthosis driven by electro-rheological fluid based actuators in *Robotics and Automation, 2005. ICRA 2005. Proceedings of the 2005 IEEE International Conference.* (IEEE), pp. 2283–2289.
39. Poon WC, Weeks ER, Royall CP (2012) On measuring colloidal volume fractions. *Soft Matter* 8(1):21–30.

Tunable Shear Thickening in Suspensions: Supplementary Information

Neil Y.C. Lin,[1] Christopher Ness,[2] Jin Sun,[2] and Itai Cohen[1]

[1]*Department of Physics, Cornell University, Ithaca, NY 14853, USA*

[2]*School of Engineering, University of Edinburgh,*

Mayfield Road, Edinburgh EH9 3JL, United Kingdom

CONTENTS

I. ORTHOGONAL SUPERPOSITION (OSP)

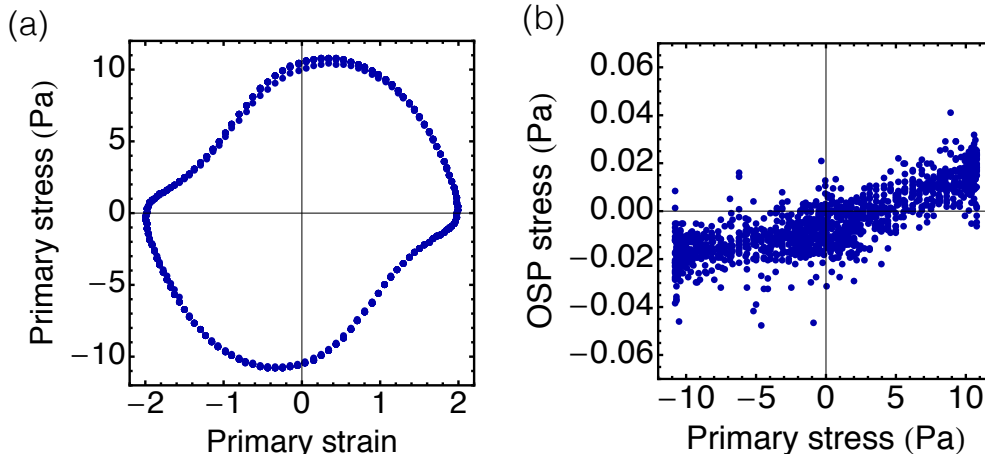## A. Calibration I: Instrumental biaxial coupling

FIG. 1. (a) Lissajous-Bowditch curve of primary stress versus strain. The stress overshoots at strain $\approx \pm 1.5$ result from the formation of particle contacts within a cycle. (b) Lissajous-Bowditch curve of OSP stress versus primary stress. The positive correlation between these two stresses implies a measurable instrumental coupling. However, the coupling $\approx 0.1\%$ is insigficant.

The instrumental coupling is closely related to the alignment between the primary and OSP driving motions of the rheometer. Therefore, the parts of the drivers have to be machined and assembled carefully. To quantify the instrumental coupling, we load a suspension into the ARES-G2 rheometer and impose a uniaxial oscillatory shear with a strain amplitude $\gamma_0 = 2$. Meanwhile, we monitor the OSP response that directly arises from the instrumental coupling. We plot the Lissajous-Bowditch (LB) curve of the primary response in Fig. 1 (a). The LB curve indicates a viscous response, in which the stress is maximal around zero strain. The stress overshoots around strain $\approx \pm 1.5$ are associated with the formation of particle frictional contacts. In Fig. 1 (b), we plot the OSP stress response versus the primary stress. Since we do not impose any OSP shear strain, the measured OSP response solely results from the coupling. We observe a positive correlation between the two stress responses implying that the coupling is finite and measurable. Nevertheless, we find this correlation remarkably small. For example, when the primary stress response is maximal (≈ 10 Pa), the OSP response is only ≈ 0.15 Pa, about 0.1% of the applied primary stress.

B. Calibration II: Uniaxial oscillatory shear

In the main draft, we show a reentrant shear thickening at large OSP amplitudes and high frequencies. The reentrant thickening should be related to the frictional contacts formed by the OSP flow when its amplitude is large. This means that under uniaxial shear, the suspension viscosity should start to increase when the applied strain amplitude exceeds a critical value. To confirm this, we repeat the frequency sweep measurement but now in the absence of the primary flow. We plot the OSP viscosity $|\eta_\perp^*|$ as a function of OSP frequency for seven different strain amplitudes $\gamma_\perp$ in Fig. 2. We find a slight frequency thinning at low frequencies that might be due to either Brownian motion or the slight attraction between particles. Nevertheless, we do observe thickening behavior at $\gamma_\perp = 5\%$ (black points). This thickening behavior is consistent with the viscosity growth observed in the biaxial case.
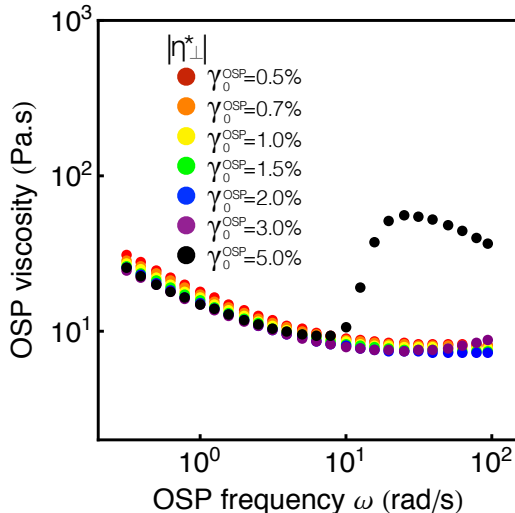

FIG. 2. OSP viscosity $|\eta_\perp^*|$ as a function of ω for seven different strain amplitudes. We do not observe any shear thickening at $\gamma_0^{\mathrm{OSP}} < 5\%$.

C. Calibration III: Viscosity standard measurement

Finally, we want to further confirm that both primary and OSP measurements of viscosity are accurate and consistent. We load a viscosity standard (CANNON N4000) into the ARES-G2 and repeat the reported biaxial experiment with exactly the same parameters.
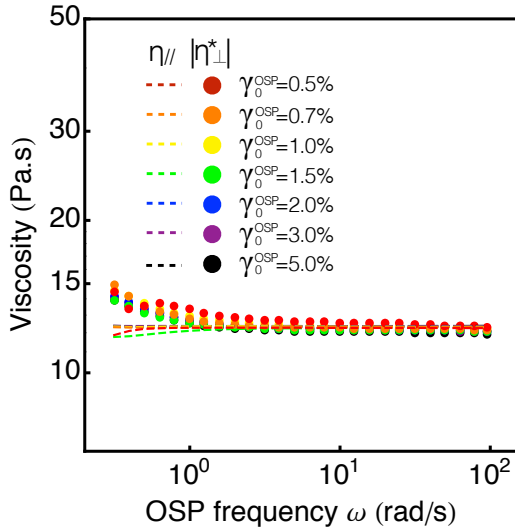
FIG. 3. Primary $\eta_{\parallel}$ and OSP $|\eta_{\perp}^*|$ viscosities versus OSP frequency ω. The primary shear rate is 0.2 s^{-1}.

The tested viscosity standard has a nominal viscosity ~ 12 Pa.s at room temperature, which is similar to our suspension viscosity. For a coupling- and artifact-free measurement, the measured viscosity should be Newtonian, hence independent of the OSP frequency and amplitude. We show the viscosity in Fig. 3. Overall both the primary (dashed lines) and OSP (dots) viscosities match each other, and remain constant throughout all frequencies and amplitudes. We observe higher viscosities at low OSP frequencies suggesting that the viscosities are overestimated by the instrument (by $\approx 13\%$). While this small viscosity should be further corrected in future experiments, it is insignificant and should not alter the main trend of the reported biaxial data.

D. Speaker-motor OSP

We use a subwoofer to provide vibration orthogonal to the rotation direction of the motor gear. To maintain the vibration speed, $A\omega$ while the frequency ω is ramped up, we monitor the acceleration of the vibration $|a|$, and reduce the amplitude A accordingly. The vibration acceleration $|a| = A\omega^2 \sin(\omega t)$ is measured by a wireless accelerometer (Monnit, g-force max and avg). At $\omega = 250$ Hz, the vibration amplitude is approximately 13 μm.

The suspension tested in this experiment is cornstarch in water with a weight concen-

4

tration $\approx 55\%$. Although the solvent's density does not match the cornstarch density, our experiment time is short (≈ 3 min), so we do not observe any time-dependent behavior associated with sedimentation. We film the gear rotation with a camera at a frame rate 240 fps. This high frame rate allows us to determine the real-time speed of the motor. To do so, we analyze the local image region of the gear using "Digital Image Correlation" [1, 2] extracting the instantaneous rotation speed.
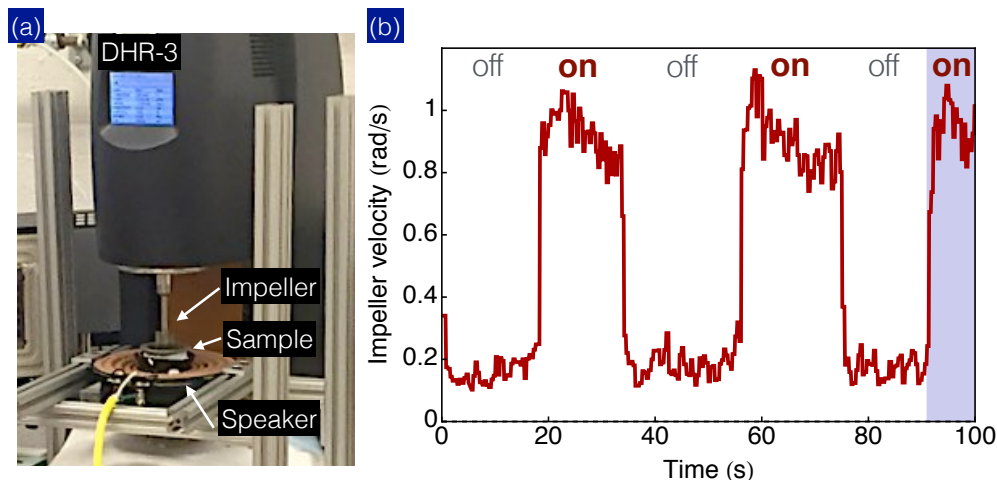
E. Speaker-rheometer OSP

FIG. 4. (a) We mount a subwoofer on a stress-controlled rheometer (TA-Instrument DHR-3) to provide OSP flows. The sample holder is epoxied to the hollow speaker cone. (b) As the speaker is switched on (purple shades), the impeller rotation speed increases by approximately five times.

In the speaker-motor OSP experiment, the motor stalls when the resistance reaches its stalling torque. Such a rotation cessation can be confused with the shear jamming phenomena found in even denser suspensions or granular systems. To clarify this issue, we mount the subwoofer on a stress-controlled rheometer (TA-Instrument DHR-3), and monitor the rotation speed of the impeller (vane rotor) as we switch on/off the speaker. The blades of the impeller are thin minimizing the squeezing flow caused by the vertical vibration. We fix the applied torque at 1 mN.m, in which our cornstarch sample shows a clear shear thickening behavior. The schematic of the setup is shown in Fig. 4 (a). We set the speaker vibration frequency ≈ 500 Hz to provide a vibration speed comparable to the primary shear rate with

5

a reasonably small oscillation amplitude. As shown in Fig. 4(b), the impeller rotates about five times faster when we turn on the speaker. More importantly, when the speaker is off, the impeller rotates at a slower speed rather than completely stop. This finding confirms that the suspension state is in the DST regime. We also find that the transition between slow and fast rotations is reversible, consistent with our speaker-motor tests and biaxial shear experiments.

II.   SAMPLE CHARACTERIZATION AND DETAILS

A.   Structure – confocal images

The solvent (Dipropylene glycol) used in the experiment has a refractive index (1.439) that nearly matches the index of the silica particles (1.435). This index match minimizes the van-der waals force between particles [3] and allows us to perform direct imaging of the suspension structure [4–6]. Furthermore, a small amount of fluorescein salt is added in the sample to dye the solvent and reduce the Debye length of the electrostatic force. We then use a confocal microscope to examine the structure and volume fraction of a quiescent suspension sample. We show the confocal images sliced along three different axes in Fig. 5(a). We also show a 3D reconstruction of the image stack in Fig. 5(b). From the images, we do not observe any aggregation of particles over time, implying that the suspension is well stabilized by the electrostatic force. We also find that the suspension structure remains disordered at high volume fractions. Finally, we use the 3D images to estimate the suspension volume fraction by counting particles, and find the volume fraction consistent with that calculated according to the weight ratio.

The used solvent Dipropylene glycol also has a low vapor pressure minimizing the evaporation rate [7]. By monitoring the viscosity of the suspension over time, we find that the sample's volume fraction remains constant throughout the entire experiment. Furthermore, we use micron-sized particles to reduce sedimentation effect.

B.   Stress and rate sweep plots

The rheometer used in the biaxial experiment is strain-controlled. The strain-controlled mode ensures the accuracy of the applied OSP strain. In previous literature, however,
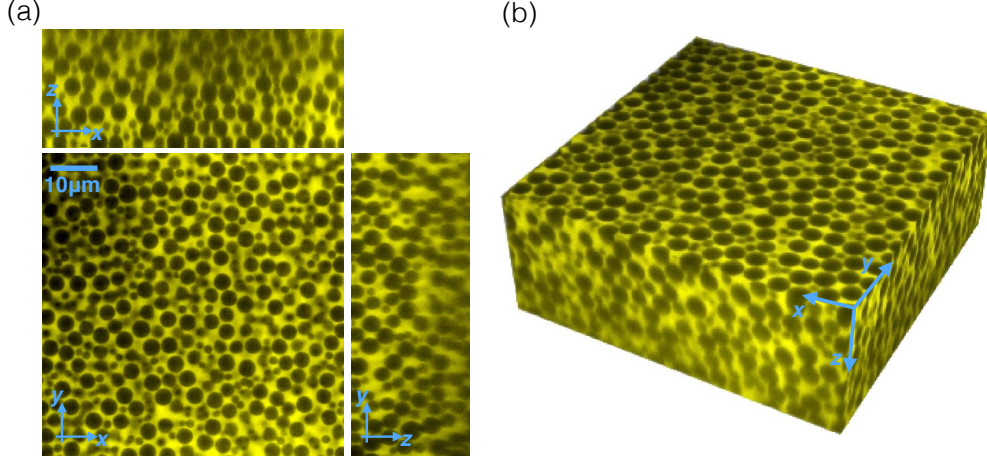
FIG. 5. (a) Three different slices from a 3D image matrix of the tested binary suspension. The middle, top, and right images correspond to the top $(\hat{x}\hat{y})$, front $(\hat{x}\hat{z})$, and side views $(\hat{y}\hat{z})$, respectively. The solvent is dyed with fluorescein salt, so it appears bright. The silica particles are not fluorescently labeled, so they appear dark. (b) 3D reconstruction of the image stack. The deeper image region (larger z value) gets blurrier due to the spherical aberration and its resulting point-spread-function. We do not observe significant crystallization in the sample.
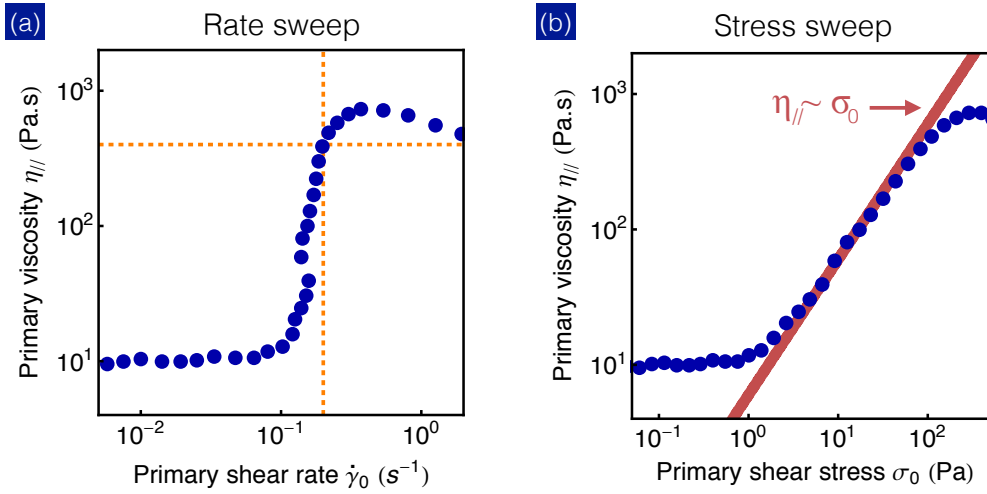
FIG. 6. (a) Primary viscosity $\eta_{\parallel}$ as a function of shear rate. We see an abrupt increase in $\eta_{\parallel}$ at $\dot{\gamma}_0 \approx 0.1$. The dashed lines denote the primary shear rate and its corresponding viscosity in biaxial experiment. (b) Data from (a) but in a stress-sweep fashion. Consistent with previous works [8], we observe a nearly linear increase in viscosity $\eta_{\parallel} \propto \sigma_0^{0.95}$ in the DST regime. The red line denotes a linear response $\eta_{\parallel} \propto \sigma_0$.

7

it has been shown that uniaxial shear thickening is a stress-controlled phenomena [8–10]. Many previous works have presented the viscosity data as a function of stress. Therefore, to characterize the uniaxial thickening behavior of our sample, we perform a stress sweep measurement and plot the same dataset in both stress and strain sweep fashions. The measurement is performed using an Anton Paar MCR 301 stress-controlled rheometer. In Fig. 6(a) and (b) we show the rate and stress sweep data for our discontinuous thickening sample, respectively. The orange dashed lines in Fig. 6(a) indicate the primary shear rate employed in the biaxial experiment and its corresponding shear viscosity. In the stress sweep plot (Fig. 6(b)), we find that $\eta_\parallel \propto \sigma_0^{0.95}$, depicting a nearly DST behavior [8]. Put differently, $\sigma_0 = \eta_\parallel \dot{\gamma}_0$ is almost linear in $\eta_\parallel$, signifying that stress takes a range of values at fixed strain rate which is the defining discontinuity property of DST.

C. OSP phase angle
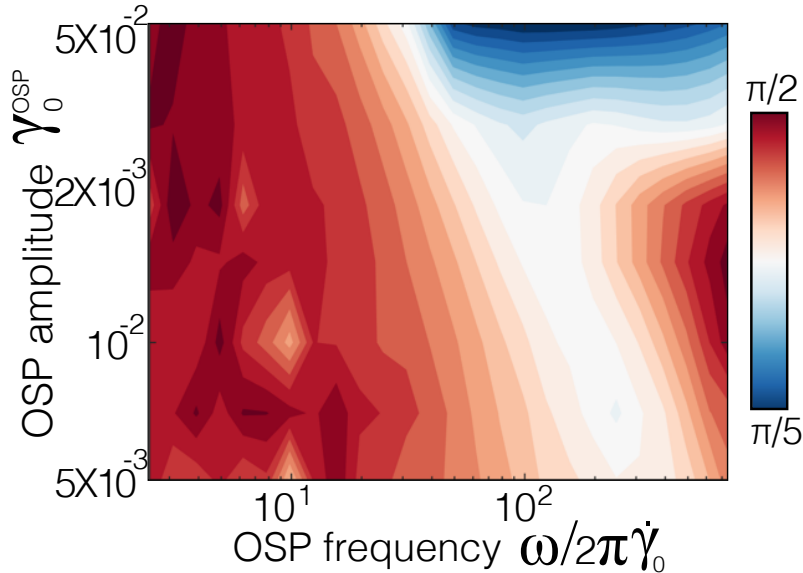
FIG. 7. Contour plot of phase angle δ between OSP stress and strain. The response at low frequencies and strain amplitudes is viscous ($\delta \approx \pi/2$). The response in the reentrant thickening regime is elastic ($\delta \approx 0$). The trend of $\delta(\omega/2\pi\dot{\gamma}_0)$ at $\gamma_0^{\mathrm{OSP}} \leq 0.002$ is non-monotonic.

The oscillatory OSP flow allows us to probe both the overall viscosity magnitude $|\eta_\perp^*|$ and the phase angle δ between the stress and strain. The latter information describes the

viscoelasticity of the sample, in which $\delta = \pi/2$ and $\delta = 0$ correspond to viscous and elastic responses, respectively. We report the overall viscosity magnitude $|\eta_\perp^*|$ in the main text. Here, we show the phase angle as a function of OSP strain amplitude and frequency in Fig. 7. We find that in the instantaneous adaptation regime, the OSP stress response is mainly viscous. This finding suggests that the alignment of the force chain regulated by the ratio $\dot{\gamma}_{\mathrm{OSP}}/\dot{\gamma}_0$, consistent with our simulation results reported in the main manuscript Fig. 2. As the OSP frequency increases, δ decays implying a more elastic stress response. The transition from viscous to elastic response characterizes the competition between the primary and OSP shear rates. Surprisingly, this transition trend $\delta(\omega/2\pi\dot{\gamma}_0)$ is non-monotonic, suggesting that the mechanisms of "chain tilting" (OSP rate comparable to primary rate) and "chain breaking" (OSP rate dominates) regimes should be distinct. At large amplitudes and high frequencies, where the reentrant thickening emerges, we observe small $\delta \approx \pi/5$ denoting an elastic response. In this regime, the OSP flow is strong enough to form force chains by itself. Therefore, the stress is largely transmitted through the OSP force chains, and demonstrates a primarily elastic response.

D. Solvent viscosity

To characterize the viscosity of the used solvent (Dipropylene glycol) we perform rate sweep measurements at ten different temperatures ranging from -1°C to 30°C. The viscosity is plotted as a function of shear rate in Fig. 8(a). We find that Dipropylene glycol displays a Newtonian behavior at all shear rates and temperatures. This Newtonian behavior ensures that the interparticle hydrodynamic interaction in our tested shear thickening samples has a conventional form of lubrication force. We further read out the mean viscosity value for each temperature and plot the result in Fig. 8(b). We find that the viscosity increases significantly as the temperature drops. In experiment, we set the temperature at 20°C throughout all measurements.

III. INSTANT ADAPTATION AND ISOTROPIC VISCOSITY

In the instant adaptation regime, force chains always align with the net compressive axis. Therefore, the chain alignment demonstrates a viscous response to the applied OSP flow
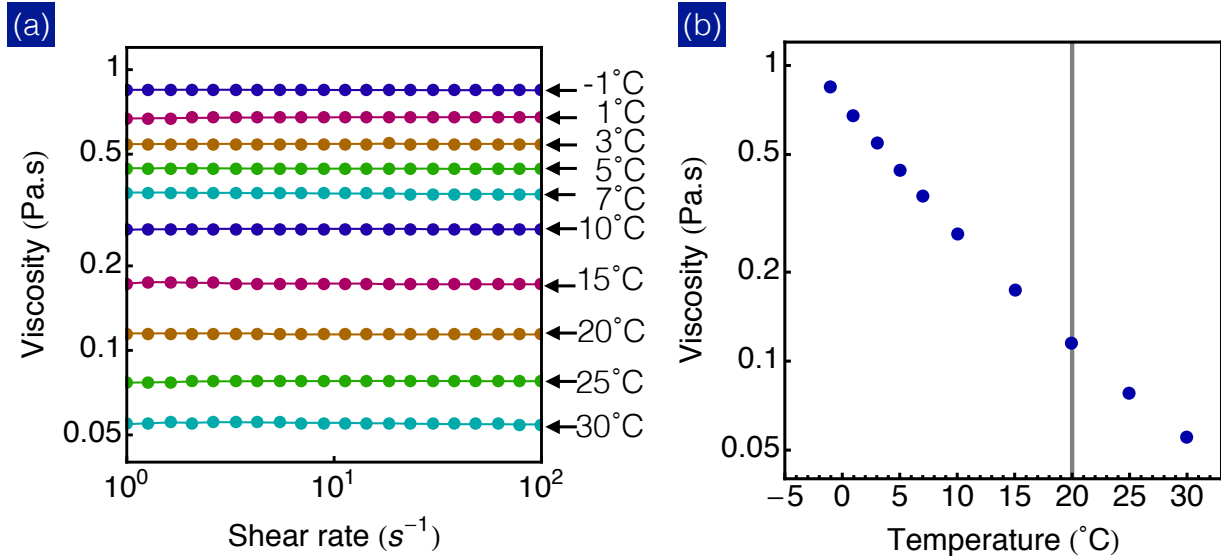
FIG. 8. Shear rate sweep measurements of Dipropylene glycol viscosity for ten different environmental temperatures. We find the solvent remains Newtonian at all explored shear rates and temperatures. (b) Mean viscosity (averaged over rates) plotted as a function of temperature. The vertical line denotes the temperature $20°C$ maintained throughout all experiments in the main manuscript.

$(\phi \propto \dot{\gamma}^{\text{OSP}})$ as shown in the main manuscript Fig. 2(a). This instant adaptation directly implies an isotropic viscosity response of the thickening suspension. We provide a simple mathematical argument elucidating this relation.

The magnitude of the overall shear rate can be written as:

$$\dot{\gamma}_{\text{tot}} = \sqrt{\dot{\gamma}_0^2 + (\dot{\gamma}_0^{\text{OSP}} \cos(\omega t))^2} \approx \dot{\gamma}_0 + \mathcal{O}((\dot{\gamma}_0^{\text{OSP}})^2). \tag{1}$$

Since the chain angle ϕ remains small, it can be approximated as:

$$\phi = \tan^{-1}\left(\frac{\dot{\gamma}_0^{\text{OSP}} \cos(\omega t)}{\dot{\gamma}_0}\right) \approx \frac{\dot{\gamma}_0^{\text{OSP}} \cos(\omega t)}{\dot{\gamma}_0} \tag{2}$$

when the OSP shear rate is small $\dot{\gamma}_0^{\text{OSP}} \cos(\omega t) \ll \dot{\gamma}_0$. The approximately constant strain rate (to leading order) results in a shear stress that is constant in magnitude but of variable orientation. The magnitude of the net shear stress is $\sigma_{uz} = \eta \dot{\gamma}_0$, where $\hat{u}\hat{z}$ is the shear plane of the combined flows, and η is the uniaxial thickening viscosity without orthogonal perturbation. To calculate the primary and OSP stresses measured in experiment, we then project the net stress, which is aligned along $\hat{u}\hat{z}$ axis, back to $\hat{x}\hat{z}$ and $\hat{y}\hat{z}$. The projected

10

stresses $\sigma_\parallel = \sigma_{xz}$, and $\sigma_\perp = \sigma_{yz}$ are:

$$\sigma_\parallel = \sigma_{uz}\cos(\phi) \approx \eta\dot{\gamma}_0 + \mathcal{O}(\phi^2)$$

$$\sigma_\perp = \sigma_{uz}\sin(\phi) \approx \eta\dot{\gamma}_0\phi + \mathcal{O}(\phi^3) \quad .$$

From Eq.2, $\sigma_\perp$ can be further reduced to $\sigma_\perp \approx \eta\dot{\gamma}_0^{\mathrm{OSP}}\cos(\omega t)$. Collectively, we find that both primary $\eta_\parallel = \sigma_\parallel/\dot{\gamma}_0$ and OSP $\eta_\perp = \sigma_\perp/\left[\dot{\gamma}_0^{\mathrm{OSP}}\cos(\omega t)\right]$ viscosities coincide the original uniaxial viscosity η. The result also suggests a viscous OSP stress response, consistent with the phase angle measurement reported in Sec. II C.

IV. SIMULATION DETAILS

A. Numerical model

The simulation model used in the present work is implemented in the open source molecular dynamics package LAMMPS [11], and has been employed previously in the study of shear thickening suspensions as described in Ref [12].

The equations of motion for non-Brownian particles suspended in a fluid can be written simply as [13]

$$m\frac{d}{dt}\begin{pmatrix}\mathbf{v}\\\boldsymbol{\omega}\end{pmatrix} = \sum\begin{pmatrix}\mathbf{F}\\\boldsymbol{\Gamma}\end{pmatrix}, \tag{3}$$

for particles of mass m with translational and rotational velocity vectors $\mathbf{v}$ and $\boldsymbol{\omega}$ respectively, and subjected to force and torque vectors $\mathbf{F}$ and $\boldsymbol{\Gamma}$ respectively. In this work we limit the forces and torques to those arising due to direct surface contacts between neighbouring particles ($\mathbf{F}^c, \boldsymbol{\Gamma}^c$) and those arising through short range, pairwise, hydrodynamic lubrication forces ($\mathbf{F}^l, \boldsymbol{\Gamma}^l$). For an interaction between particles i and j, the force and torque due to hydrodynamics can therefore be expressed as

$$\begin{aligned}\mathbf{F}^l_{ij} = &-a_{sq}6\pi\eta_f(\mathbf{v}_i - \mathbf{v}_j)\cdot\mathbf{n}_{ij}\mathbf{n}_{ij}\\&-a_{sh}6\pi\eta_f(\mathbf{v}_i - \mathbf{v}_j)\cdot(\mathbf{I} - \mathbf{n}_{ij}\mathbf{n}_{ij}),\end{aligned} \tag{4a}$$

$$\begin{aligned}\boldsymbol{\Gamma}^l_{ij} = &-a_{pu}\pi\eta_f d_i^3(\boldsymbol{\omega}_i - \boldsymbol{\omega}_j)\cdot(\mathbf{I} - \mathbf{n}_{ij}\mathbf{n}_{ij})\\&-\frac{d_i}{2}\left(\mathbf{n}_{ij}\times\mathbf{F}^l_{ij}\right).\end{aligned} \tag{4b}$$

for a suspending fluid of viscosity η_f, where $\mathbf{n}_{ij}$ is the vector pointing from particle j to particle i, and with squeeze a_{sq}, shear a_{sh} and pump a_{pu} resistance terms as derived by Kim and Karrila [14] and given in Eq 5 for particle diameters d_i and d_j, with $\beta = d_j/d_i$:

11

$$a_{sq} = \frac{\beta^2}{(1+\beta)^2} \frac{d_i^2}{2h_{\text{eff}}} + \frac{1+7\beta+\beta^2}{5(1+\beta)^3} \frac{d_i}{2} \ln\left(\frac{d_i}{2h_{\text{eff}}}\right)$$
$$+ \frac{1+18\beta-29\beta^2+18\beta^3+\beta^4}{21(1+\beta)^4} \frac{d_i^2}{4h_{\text{eff}}} \ln\left(\frac{d_i}{2h_{\text{eff}}}\right), \tag{5a}$$

$$a_{sh} = 4\beta \frac{2+\beta+2\beta^2}{15(1+\beta)^3} \frac{d_i}{2} \ln\left(\frac{d_i}{2h_{\text{eff}}}\right)$$
$$+ 4\frac{16-45\beta+58\beta^2-45\beta^3+16\beta^4}{375(1+\beta)^4} \frac{d_i^2}{4h_{\text{eff}}} \ln\left(\frac{d_i}{2h_{\text{eff}}}\right), \tag{5b}$$

$$a_{pu} = \beta \frac{4+\beta}{10(1+\beta)^2} \ln\left(\frac{d_i}{2h_{\text{eff}}}\right)$$
$$+ \frac{32-33\beta+83\beta^2+43\beta^3}{250\beta^3} \frac{d_i}{2h_{\text{eff}}} \ln\left(\frac{d_i}{2h_{\text{eff}}}\right). \tag{5c}$$

For each interaction, the particle pair surface-to-surface distance h is calculated according to $h = |\mathbf{r}_{ij}| - \frac{d_i+d_j}{2}$, for centre-to-centre vector $\mathbf{r}_{ij}$. Recent experimental [9] and computational [15] work indicates that direct particle-particle contacts contribute significantly to the suspension viscosity, in addition to hydrodynamics. To permit such contacts in the present model, we truncate the lubrication divergence at $h_{\text{min}} = 0.001d_{ij}$ (for weighted average particle diameter $d_{ij} = \frac{d_i d_j}{d_i+d_j}$), i.e., setting $h = h_{\text{min}}$ in the force calculation, when $h < h_{\text{min}}$. The effective interparticle gap used in the force calculation, h_{eff}, is therefore given by

$$h_{\text{eff}} = \begin{cases} h & \text{for } h > h_{\text{min}} \\ h_{\text{min}} & \text{otherwise.} \end{cases} \tag{6}$$

For computational efficiency, the lubrication forces are omitted when the interparticle gap h is greater than $h_{\text{max}} = 0.05d_{ij}$. The volume fraction is sufficiently high that all particles have numerous neighbours within this range, and we verified, therefore, that such an omission is inconsequential to the dynamics. When the lubrication force is overcome and particle surfaces come into contact, their interaction is defined according to a linear spring model [16], with normal ($\mathbf{F}^{c,n}$) and tangential ($\mathbf{F}^{c,t}$) force and torque $\mathbf{\Gamma}^c$ given by

$$\mathbf{F}_{ij}^{c,n} = k_{\text{n}}\delta\mathbf{n}_{\text{ij}}, \tag{7a}$$

$$\mathbf{F}_{ij}^{c,t} = -k_{\text{t}}\mathbf{u}_{\text{ij}}, \tag{7b}$$

$$\mathbf{\Gamma}_{ij}^c = -\frac{d_i}{2}(\mathbf{n}_{ij} \times \mathbf{F}_{ij}^{c,t}), \tag{7c}$$

for a collision between particles i and j with normal and tangential spring stiffnesses k_n and k_t respectively, particle overlap δ (equal to $-h$) and tangential displacement $\mathbf{u}_{\text{ij}}$. We note
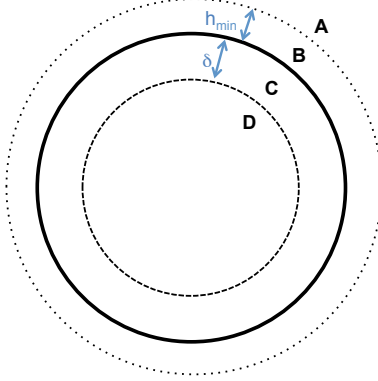
12

FIG. 9. Illustration of interaction lengthscales (not to scale). Forces resolved in region A: $\mathbf{F}^l_{ij}(h_{\text{eff}} = h)$; B: $\mathbf{F}^l_{ij}(h_{\text{eff}} = h_{\text{min}})$; C: $\mathbf{F}^l_{ij}(h_{\text{eff}} = h_{\text{min}}) + \mathbf{F}^c_{ij}(\mu_p = 0)$; D: $\mathbf{F}^l_{ij}(h_{\text{eff}} = h_{\text{min}}) + \mathbf{F}^c_{ij}(\mu_p = 1)$.

that the damping arising from the hydrodynamics is always sufficient to achieve a steady state without employing a thermostat, and further damping in the particle contact model is omitted for simplicity.

To regulate the particle-particle tangential forces, we employ the Critical Load Model (CLM) for particle-particle friction [15, 17]. This model gives an additional stress scale for the particle interaction, which, numerically, is the origin of the onset stress for shear thickening σ^* [9]. An interparticle static Coulomb friction coefficient μ_p is defined according to $|\mathbf{F}^{c,t}_{i,j}| \leq \mu_p|\mathbf{F}^{c,n}_{i,j}|$, setting a maximum value for the tangential force during a collision. In granular systems, μ_p consequently determines the volume fraction at which flow arrest or jamming will occur [18]. For each pairwise collision, the value of μ_p is dependent upon the normal force between the interacting particles and some critical normal force magnitude F^{CL}, such that

$$\mu_p = \begin{cases} 1 \ \ \text{for} \ |\mathbf{F}^{c,n}_{i,j}| > F^{CL} \\ 0 \ \ \text{otherwise} \end{cases}. \tag{8}$$

As a result of the CLM, particles that interact through weak forces, i.e. collisions where $\delta \to 0$, are frictionless, while interactions with large normal forces are frictional. The particle overlaps required to exceed F^{CL} are, at their absolute maximum, of order $10^{-5}d_{ij}$. An overview of the interaction lengthscales is given in Fig 9. In principle, h_{min} and δ might serve as tuning parameters that may be chosen to reflect details of a suspension of interest. For example, particles with particularly long-range repulsion or long stabilising polymer hairs or those with prominent asperities or complex surface topology might be better captured by

13

large $h_{\min}$. In practice, however, we find that provided $h_{\min} \leq 0.005d$, steady state dynamics are little changed as $h_{\min} \to 0$. Similarly there is little dependence on δ, provided $0 < \delta \ll d$.

Forces calculated according to the above models may then be summed for each particle pair to give the total force and torque $\mathbf{F}_{ij}$ and $\mathbf{\Gamma}_{ij}$, respectively. Particle positions and velocities are then updated according to a time stepping scheme, by summing contributions from all pairwise forces and solving Equation 3 numerically.

Isotropic particle assemblies with minimised particle-particle overlaps are generated in a 3-dimensional periodic domain of volume V. It is determined that $O(10^3)$ spheres are sufficient to capture the bulk rheology and microstructural phenomena independently of system size. Bidispersity at a diameter ratio of $1 : 1.4$ and volume ratio of $1 : 1$ is used to minimize crystallization during flow [19] (and references therein).

The 3×3 stress tensor is constructed from the particle pair force data, and given by:

$$\mathbf{\sigma} = \frac{1}{V} \sum_i \sum_{i \neq j} \mathbf{r}_{ij} \mathbf{F}_{ij}. \tag{9}$$

Data from 20 realizations with randomized initial particle positions are used to obtain ensemble-averaged stresses.

B. Key assumptions of the simulation model and potential sources of discrepancy

1) Full solution of the long and short range hydrodynamic forces, essential for a truly accurate resolution of the fluid effects, has traditionally been achieved using the Stokesian Dynamics algorithm [20], though its great computational expense makes large (or very dense) simulations challenging and time consuming. For highly packed suspensions, where interparticle gap sizes tend to 0, the divergent lubrication forces between extremely close particles dominate the hydrodynamic interaction, so $\mathbf{F}^l$, $\mathbf{\Gamma}^l$ can be approximated by summing pairwise lubrication forces among nearest neighbouring particles. This simplification is becoming a conventional approach for modelling very dense suspended systems [15, 21–23]. A further assumption of the lubrication approximation is that the fluid may permeate the matrix formed by solid particles at infinite rate. For the system size used in the present work, and considering the periodicity of the box, it is assumed that there are no spatial or temporal variations of local volume fraction, so the effects of fluid migration are likely to be negligible.

14

2) The present simulation model allows particle inertia, but fluid inertia is neglected for simplicity. The flow induced by the primary shearing with rate $\dot{\gamma}_0$ has Stokes number $\rho\dot{\gamma}_0 d_{ij}^2/\eta_f \ll 1$ such that inertia is not relevant. The OSP flow however, has larger Stokes numbers, with $\rho\dot{\gamma}_{\text{OSP}} d_{ij}^2/\eta_f \to 0.1$ for the case where $\gamma_{\text{OSP}} = 5\%$, such that inertia may begin to become important. This may account for the discrepancy between simulation and experiment in this case. Trulsson [23] demonstrated that for inertial suspension flows, the dissipation through particle contacts considerably outweighs that due to fluid effects, which we take as justification of the present model. In addition, the scaling laws predicted by the present simulation model and published elsewhere [24] (specifically $\sigma_{xy} \propto \dot{\gamma}$ and $\sigma_{xy} \propto \dot{\gamma}^2$ for viscous and inertial flows respectively) are consistent with observations from comparable experiments [25, 26].

3) The employed friction model may be considered to account for roughness on the surface of ideal spheres in model systems, but neglects the resistance to rolling offered by particle asphericity. For less idealised cases, such as cornstarch suspensions, further computational tools such as bonded-sphere complex particle shapes and rolling resistance coefficients are currently being pursued as means of accounting for severe asphericity in addition to surface roughness. It is anticipated that enhanced interlocking in such cases will cause shear thickening to be exaggerated even further.

4) $\mu_p = 1$ is chosen to represent a highly frictional near-upper limiting case. In practice, μ_p can be chosen to represent the roughness of any particles of interest. The primary effect of varying μ_p is to alter the volume fraction at which the viscosity will diverge in the frictional limit. A secondary consequence of this is that at fixed volume fraction, the extent of shear thickening, i.e. the step change in viscosity upon exceeding σ^*, will decrease as $\mu_p \to 0$. Note that σ^* and $\dot{\gamma}_0$ are not functions of μ_p. These properties of μ_p have been reported recently elsewhere [17].

C. "Uniaxial" shear rheology predicted by the simulation model

Inclusion of the CLM introduces a simulation timescale associated with the shear thickening onset stress σ^*, which can be written as $1/\dot{\gamma}^* = \frac{3}{2}\pi\eta_f d_{ij}^2/F^{CL}$ [17]. An assembly of particles described by the above interaction models is sheared at controlled rate (with flow
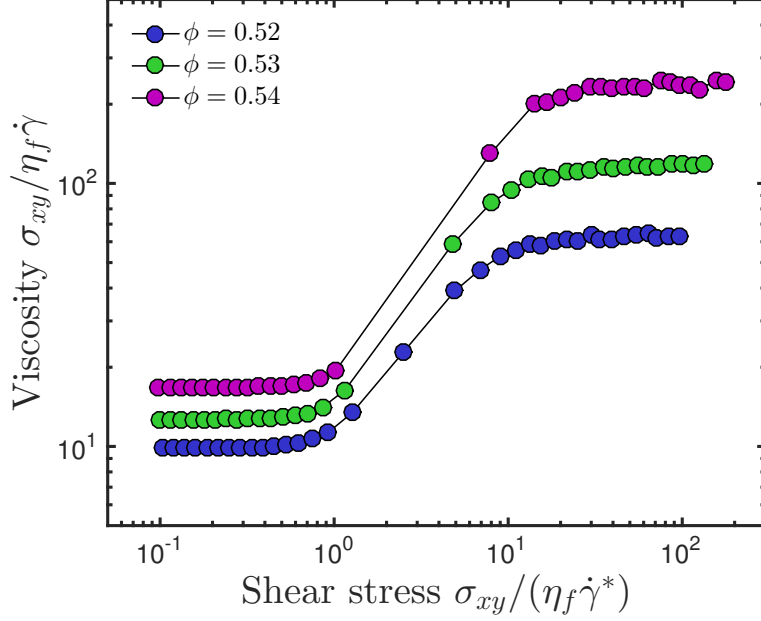
15

FIG. 10. Simple shear rheology predicted by the simulation model used in this work. The suspension shear thickens above a critical stress $\sigma_{xy}/(\eta_f \dot{\gamma}^*) \approx 1$.

in x, gradient in y and vorticity in z), with the dimensionless rate $\dot{\gamma}/\dot{\gamma}^*$ varied across orders of magnitude. The rheological flow map is presented in Fig 10, where σ_{xy} is the relevant component of $\boldsymbol{\sigma}$ (Equation 9) to represent the shear stress. Shear thickening is observed above a critical stress $\sigma_{xy}/(\eta_f \dot{\gamma}^*) \approx 1$. The results in the main part of the present paper are all obtained in the limit of large $\dot{\gamma}/\dot{\gamma}^*$, where $\dot{\gamma}$ is analogous to the *primary* shearing flow, and where the suspension would be expected to flow well within the shear thickened regime.

[1] J Kristian Sveen and Edwin A Cowen. Quantitative imaging techniques and their application to wavy flows. *Advances in Coastal and Ocean Engineering*, 9:1, 2004.

[2] Rafael C Gonzalez and Richard E Woods. Image segmentation: Region-oriented segmentation. *Digital Image Processing, Addison-Wesley Publishing Company, Inc*, pages 458–462, 1992.

[3] Daniel Bonn, Jakub Otwinowski, Stefano Sacanna, Hua Guo, Gerard Wegdam, and Peter Schall. Direct observation of colloidal aggregation by critical casimir forces. *Physical review letters*, 103(15):156101, 2009.

[4] Neil YC Lin, Jonathan H McCoy, Xiang Cheng, Brian Leahy, Jacob N Israelachvili, and Itai Cohen. A multi-axis confocal rheoscope for studying shear flow of structured fluids. *Review of Scientific Instruments*, 85(3):033905, 2014.

[5] Vikram Prasad, D Semwogerere, and Eric R Weeks. Confocal microscopy of colloids. *Journal of Physics: Condensed Matter*, 19(11):113102, 2007.

[6] Anthony D Dinsmore, Eric R Weeks, Vikram Prasad, Andrew C Levitt, and David A Weitz. Three-dimensional confocal microscopy of colloids. *Applied optics*, 40(24):4152–4159, 2001.

[7] RL Smith. Review of glycol ether and glycol ether ester solvents used in the coating industry. *Environmental health perspectives*, 57:1, 1984.

[8] Eric Brown and Heinrich M Jaeger. Shear thickening in concentrated suspensions: phenomenology, mechanisms and relations to jamming. *Reports on Progress in Physics*, 77(4):046602, 2014.

[9] B M Guy, M Hermes, and W C K Poon. Towards a Unified Description of the Rheology of Hard-Particle Suspensions. *Physical Review Letters*, 115(8):88304, 2015.

[10] Neil YC Lin, Ben M Guy, Michiel Hermes, Chris Ness, Jin Sun, Wilson CK Poon, and Itai Cohen. Hydrodynamic and contact contributions to continuous shear thickening in colloidal suspensions. *Physical review letters*, 115(22):228304, 2015.

[11] Steve Plimpton. Fast Parallel Algorithms for Short Range Molecular Dynamics. *Journal of Computational Physics*, 117(June 1994):1–42, 1995.

[12] Christopher Ness and Jin Sun. Shear thickening regimes of dense non-Brownian suspensions. *Soft Matter*, 12(3):914–24, jan 2016.

[13] J F Brady and G Bossis. Stokesian Dynamics. *Annual Review of Fluid Mechanics*, 20(1):111–157, jan 1988.

[14] Sangtae Kim and Seppo Karrila. *Microhydrodynamics: Principles and selected applications.* Dover publications, 1991.

[15] Ryohei Seto, Romain Mari, Jeffrey F. Morris, and Morton M. Denn. Discontinuous Shear Thickening of Frictional Hard-Sphere Suspensions. *Physical Review Letters*, 111:218301, 2013.

[16] P A Cundall and O D L Strack. A discrete numerical model for granular assemblies. *Geotechnique*, 29(1):47–65, 1979.

[17] Romain Mari, Ryohei Seto, Jeffrey F Morris, and Morton M Denn. Shear thickening, frictionless and frictional rheologies in non-Brownian suspensions. *Journal of Rheology*, 58(6):1693–1724, nov 2014.

[18] Chaoming Song, Ping Wang, and Hernán A Makse. A phase diagram for jammed matter. *Nature*, 453(7195):629–632, may 2008.

[19] Atsushi Ikeda, Ludovic Berthier, and Peter Sollich. Unified study of glass and jamming rheology in soft particle systems. *Physical Review Letters*, 109(1):18301, jul 2012.

[20] John F Brady and Georges Bossis. The rheology of concentrated suspensions of spheres in simple shear flow by numerical simulation. *Journal of Fluid Mechanics*, 155(-1):105–129, apr 1985.

[21] R C Ball and John R Melrose. A simulation technique for many spheres in quasi-static motion under frame-invariant pair drag and Brownian forces. *Physica A Statistical and Theoretical Physics*, 247(1-4):444–472, 1997.

[22] Amit Kumar and Jonathan J L Higdon. Origins of the anomalous stress behavior in charged colloidal suspensions under shear. *Physical Review E - Statistical, Nonlinear and Soft Matter Physics*, 82(5 Pt 1):51401, nov 2010.

[23] Martin Trulsson, Bruno Andreotti, and Philippe Claudin. Transition from the Viscous to Inertial Regime in Dense Suspensions. *Physical Review Letters*, 109(11):118305, sep 2012.

[24] Christopher Ness and Jin Sun. Flow regime transitions in dense non-Brownian suspensions: Rheology, microstructural characterization, and constitutive modeling. *Physical Review E*, 91(1):12201, jan 2015.

[25] Abdoulaye Fall, Anaël Lemaître, François Bertrand, Daniel Bonn, and Guillaume Ovarlez. Shear thickening and migration in granular suspensions. *Physical Review Letters*, 105:268303,

2010.

[26] R. A. Bagnold. Experiments on a Gravity-Free Dispersion of Large Solid Spheres in a Newtonian Fluid under Shear. *Proceedings of the Royal Society A: Mathematical, Physical and Engineering Sciences*, 225(1160):49–63, 1954.